TU Delft

Delft University of Technology

Document Version
Final published version

Licence
CC BY

Citation (APA)
Li, L., & Voskov, D. (2021). A novel hybrid model for multiphase flow in complex multi-scale fractured systems. *Journal of Petroleum Science and Engineering*, *203*, 1-13. Article 108657. https://doi.org/10.1016/j.petrol.2021.108657

Important note
To cite this publication, please use the final published version (if applicable).
Please check the document version above.

Copyright
In case the licence states “Dutch Copyright Act (Article 25fa)”, this publication was made available Green Open Access via the TU Delft Institutional Repository pursuant to Dutch Copyright Act (Article 25fa, the Taverne amendment). This provision does not affect copyright ownership.
Unless copyright is transferred by contract or statute, it remains with the copyright holder.

Sharing and reuse
Other than for strictly personal use, it is not permitted to download, forward or distribute the text or part of it, without the consent of the author(s) and/or copyright holder(s), unless the work is under an open content license such as Creative Commons.

Takedown policy
Please contact us and provide details if you believe this document breaches copyrights.
We will remove access to the work immediately and investigate your claim.

This work is downloaded from Delft University of Technology.

Journal of Petroleum Science and Engineering 203 (2021) 108657

Contents lists available at ScienceDirect

Journal of Petroleum Science and Engineering

journal homepage: http://www.elsevier.com/locate/petrol

A novel hybrid model for multiphase flow in complex multi-scale fractured systems

Longlong Li [a,b,c,**], Denis Voskov [c,d,*]

[a] College of Science and Engineering, Hamad Bin Khalifa University, Education City, Qatar Foundation, Doha, Qatar
[b] China University of Petroleum (East China), Research Centre of Multiphase Flow in Porous Media, Qingdao, 266580, China
[c] Delft University of Technology, Department of Geoscience & Engineering, Stevinweg 1, 2628, CN, Delft, Netherlands
[d] Department of Energy Resources Engineering, School of Earth Sciences, Stanford University, 367 Panama Street, 065 Stanford, CA, 94305, United States

ARTICLE INFO

Keywords:
Reservoir simulation
Multi-level discrete fracture model
Fractured reservoir
Local-global upscaling

ABSTRACT

We present a multi-level discrete fracture model (MLDFM) to guarantee a robust and efficient solution for naturally fractured reservoir simulation. In MLDFM, we apply a triple continuum model using structured grid for forward simulation where large-scale fractures are represented with numerical embedded discrete fracture model (EDFM) and the secondary fractures are upscaled as third continuum. What makes the triple continuum model different from the previous work is that both the numerical EDFM and the third continuum are treated in a dynamic approach by considering the effect of flow direction on the complex local-scale flow response. For that purpose, we construct a finer unstructured discrete fracture matrix (DFM) grid which represents all fractures explicitly and is conformal to the boundary of coarse structured grid. During a simulation run, we apply a basis function to generate the local boundary conditions at fine scale using the global solution. Benefit from that, we can use a more accurate flow-based approach in the extended local upscaling to re-compute the transmissibility in triple continuum model. Moreover, we apply a local-global upscaling formalism to guarantee dynamically updated local boundary conditions for upscaling. Besides, we present several cases using synthetic and realistic fractured networks to demonstrate the performance of MLDFM. The results prove that the proposed MLDFM approach more accurately captures the flow in complex fractured systems than EDFM solutions by comparing against fine-scale DFM. At the same time, MLDFM is more computationally efficient in comparison with fine scale DFM.

1. Introduction

The field management is always challenging for a naturally fractured reservoir due to the complex structure of the fracture network. To address this problem, the reservoir simulation technology is taken as one of the most important tools to reduce the uncertainties underground and thus accurately predict the flow response of development strategy of interest. However, the further application of this technology is quite limited by the computational efficiency and accuracy since the structure of the fracture network could be rather complex and the fracture/fault length varies from several meters up to a few kilometers.

Since the middle of last century, researchers invested a lot of effort for the modelling of fractured reservoirs (Ramirez et al., 2009; Bourbiaux, 2010; Berre et al., 2019). Barenblatt et al. (1960) first proposed a dual-porosity (DP) model where the fractured reservoir is treated as an equivalent and homogeneous model containing matrix and fracture systems. Then Warren and Root (1963) introduced the DP into petroleum engineering. In this model, the matrix only serves as a source or sink to feed the fracture system when the fracture provides fluid-flow pathways. Moreover, it was extended as the dual-porosity dual-permeability (DPDK) model by considering the flow between matrix blocks (Gerke and van Genuchten, 1993a; Gerke and van Genuchten, 1993b; Blaskovich et al., 1983). Currently, the DP and DPDK models are widely employed by various commercial reservoir simulators and applications (Sun et al., 2013; Yao et al., 2013; Gong and Rossen, 2016). However, in both DP and DPDK models, the matrix is required to be low permeable and the fracture networks should be well connected.

Pruess and Narasimhan, 1982, 1985 proposed a multiple interacting

* Corresponding author. Delft University of Technology, Department of Geoscience & Engineering, Stevinweg 1, 2628, CN, Delft, Netherlands.
** Corresponding author. College of Science and Engineering, Hamad Bin Khalifa University, Education City, Qatar Foundation, Doha, Qatar.
E-mail addresses: lilonglong.upc@gmail.com (L. Li), D.V.Voskov@tudelft.nl (D. Voskov).

https://doi.org/10.1016/j.petrol.2021.108657
Received 29 September 2020; Received in revised form 10 February 2021; Accepted 5 March 2021
Available online 11 March 2021
0920-4105/© 2021 The Author(s). Published by Elsevier B.V. This is an open access article under the CC BY license (http://creativecommons.org/licenses/by/4.0/).

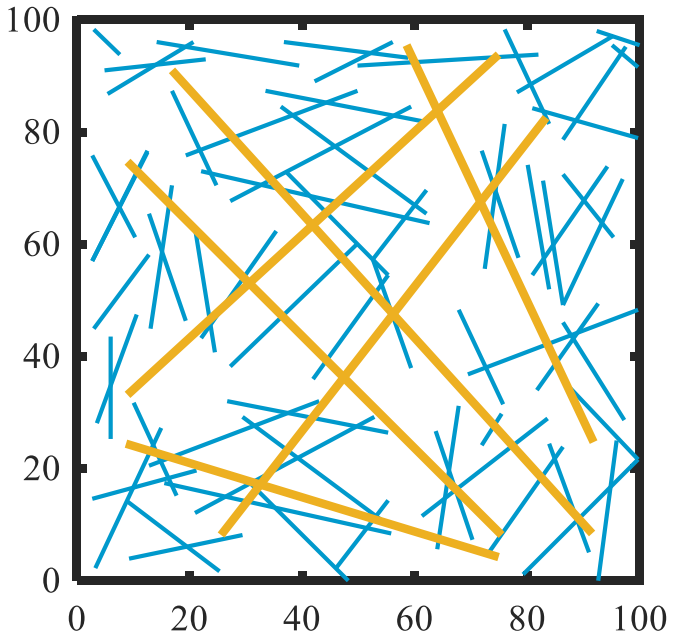

Fig. 1. A synthetic fracture network. Black thick lines are boundaries of the reservoir, blue lines represent small-scale fractures, yellow lines represent large-scale fractures. In the triple continuum model, the large-scale fractures are represented with numerical EDFM, the small-scale fractures that fall inside the same coarse structured grid are upscaled as a third continuum. (For interpretation of the references to colour in this figure legend, the reader is referred to the Web version of this article.)

continuum (MINC) model which can be interpreted as a natural extension of the dual porosity approach. Different from the DP model, the matrix blocks are discretized into a sequence of nested volume elements (Pruess, 1992). Benefit from that, the MINC model could accurately capture a transient flow within the low permeable matrix. However, being constrained by the original assumptions of the DP model, it is only applicable for well-connected fractured networks.

To break the limitations of fracture connection in DP, DPDK, and MINC, Lee et al. (2000) and Li and Lee (2008) proposed an embedded discrete fracture model (EDFM) which makes the modelling of fractured reservoirs more explicitly constrained by geological characterization based on outcrop information and reservoir measurements. Because of the flexibility of the non-conforming mesh, the EDFM is used in various applications (Fumagalli et al., 2016; Zhang et al., 2017; Hui et al., 2019; Wang et al., 2019, 2020; Yu et al., 2019). Besides, for a more flexible application of EDFM for fractures with different conductivities including barriers, Tene et al. (2017) proposed a project-embedded discrete fracture model (pEDFM).

Karimi-Fard et al. (2004) used a discrete fracture matrix (DFM) model to accurately predict the flow response in complex naturally fractured reservoirs. For explicit fracture representation, the fracture and matrix elements are conformal with each other when the fractures are represented with a lower dimension compared with the matrix grid. That makes DFM one of the most accurate representations of fractured reservoirs. However, the DFM utilization usually introduces a significant number of control volumes which reduces the efficiency of the simulation. To address this issue, the Multiple Sub-Region approach (Gong, 2007; Karimi-Fard et al., 2006; Karimi-Fard and Durlofsky, 2012, 2016; Awadalla and Voskov, 2018) was proposed where the matrix elements are aggregated as multiple sub-regions and the fracture elements are upscaled as an integrate fracture network in each coarse block. By performing local upscaling in fine DFM grid, the transmissibility among the multiple sub-regions and fracture networks can be computed. Thanks to that, the dimension of the linear system is reduced drastically when the model accurately captures the transient effect inside coarse blocks and the mass transfer between fracture and matrix. Besides, the DFM was further extended for thermal processes (Zhu et al., 2016), geomechanics treatment (Garipov et al., 2016), and even fracture propagation (Gallyamov et al., 2018; Zeng et al., 2018).

Moreover, aimed to account for the fractures in various scales efficiently and accurately, researchers proposed many hybrid models that take full advantage of above-mentioned models (Jiang and Younis, 2016; Wang et al., 2017; Ren et al., 2017; Ding et al., 2018; Xu et al., 2019; Yan et al., 2019; Guo et al., 2019; Liu et al., 2020). As proved in various applications and tests, the hybrid models have a great advantage in simulation efficiency compared with pure EDFM or DFM. However, in the hybrid models, the transmissibilities are fixed throughout the simulation. This could limit the simulation accuracy since the flow direction, that has a big effect on the local-scale flow response in complex fractured domain, cannot be fixed during a simulation of practical interest.

In this paper, we propose a novel hybrid model named multi-level discrete fracture model (MLDFM) to improve the modelling capabilities of considering the effect of flow direction on the complex local-scale flow response. For this purpose, we integrate a two-scale flow hierarchy within the naturally fractured reservoir simulation. In the coarse-scale forward simulation of a complex fracture network shown in Fig. 1, we apply a triple continuum model on a structured grid where large-scale fractures in yellow are represented with the numerical EDFM and the small-scale fractures in blue are upscaled as a third continuum. In the fine-scale simulation, we apply DFM on an unstructured grid which represents all fractures explicitly. Because of the high accuracy of DFM, the fine-scale solution is used to re-compute the transmissibility in triple continuum model through extended local upscaling. Aimed to further improve the upscaled solution, we employ global solutions from coarse-scale simulation to generate dynamically updated boundary conditions in the extended local domain. By implementing the idea in a local-global upscaling formalism, the effect of flow direction on the complex local-scale flow response can be considered in MLDFM. To demonstrate the feasibility and accuracy of MLDFM, we present several cases using synthetic fracture networks. Moreover, we test a realistic fracture network to investigate the performance of MLDFM in applied field cases.

2. Modelling approach

The proposed model is implemented using the Automatic Differentiation General Purpose Research Simulator (AD-GPRS) (Garipov et al., 2016, 2018; Voskov, 2012; Zaydullin et al., 2014). Below, we present a brief description of the MLDFM.

2.1. Conservation equations

Assuming that there are only oil and water phases in the system, the transport equations can be written as follows:

$$\frac{\partial}{\partial t}(\varphi\rho_o S_o) + \nabla\cdot(\rho_o \mathbf{u}_o) + \rho_o q_o = 0 \tag{1}$$

$$\frac{\partial}{\partial t}(\varphi\rho_w S_w) + \nabla\cdot(\rho_w \mathbf{u}_w) + \rho_w q_w = 0 \tag{2}$$

Here, φ is the reservoir porosity; t is the time; subscripts o and w indicate oil and water phases; ρ is the phase density; S is the saturation; q is the phase rate per unit volume. $\mathbf{u}_j$ is the Darcy velocity:

$$\mathbf{u}_j = -\frac{k k_{rj}}{\mu_j}\nabla P \tag{3}$$

where μ is the viscosity; k is the permeability; k_{rj} is the relative permeability of phase j; P is the pressure. Finally, we close the system using the saturation constraint:

$$S_o + S_w = 1 \tag{4}$$

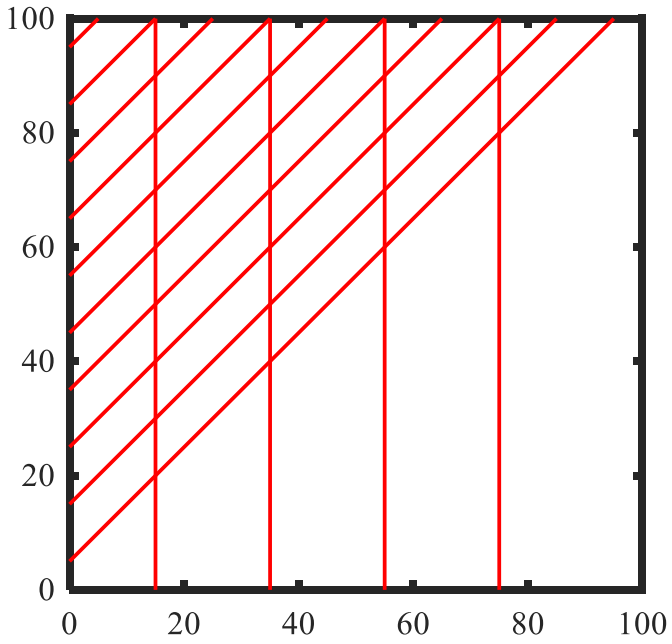

Fig. 2. A local fractured domain. The black lines are the boundaries of domain; red lines represent fractures. (For interpretation of the references to colour in this figure legend, the reader is referred to the Web version of this article.)

Table 1
Geometry parameters.

Parameter	Value	Unit
Reservoir dimensions	100 × 100	m
Reservoir thickness	10	m
Initial pressure	200	bar
Initial water saturation	0.3	
Matrix permeability	0.01	μm^2
Matrix porosity	0.2	
Fracture permeability	10,000	μm^2
Fracture porosity	1.0	
Fracture aperture	0.001	m
Well radius	0.1	m

Table 2
Fluid densities (surface condition).

Oil density (kg/m^3)	Water density (kg/m^3)
800	1000

By applying the two-point flux approximation (TPFA) for discretization in space and the backward Euler approximation for discretization in time, the transport equations shown in Eqs. (1) and (2) can be transformed as:

$$\left(V\varphi\rho_j S_j\right)^{n+1} - \left(V\varphi\rho_j S_j\right)^{n} - \Delta t\sum_l \left(\rho_j^l \lambda_j^l \gamma^l \Delta\psi^l\right)^{n+1} + \Delta t V\left(\rho_j q_j\right)^{n+1} = 0 \qquad (5)$$

Here Δt is the time step; V is the volume of a control volume; j indicates oil or water phase; $\Delta\Psi^l$ is the potential difference between two neighboring control volumes connected by l interface; $\lambda_j^l = (k_{rj}/\mu_j)^l$ is the mobility of phase j over the interface l by upstream weighting; $n+1$ is the new time step; n is the previous time step; γ is the transmissibility.

2.2. Impact of local boundary conditions

To support the motivation of the MLDFM, we investigate the effect of local boundary conditions on the flow response. Assuming a local fractured domain shown in Fig. 2, we impose two types of boundary conditions by adapting the flow direction. The reservoir and fluid parameters are taken from Table 1 through 3. The relative permeability of water is defined as $K_{rw} = S_w^2$, the relative permeability of oil is defined as $K_{ro} = S_o^2$. The first boundary condition is injecting water at the left side of the fracture network with constant pressure equal to 300 bar. The second boundary condition is injecting water at the bottom side of the fracture network with constant pressure equal to 300 bar. The simulation time is 50 days.

Table 3
Oil formation volume and viscosity.

Pressure (bar)	Formation volume (rm^3/sm^3)	Viscosity (cP)
50.0	1.97527	0.21564
70.0	1.96301	0.21934
90.0	1.95464	0.21981
110.0	1.93391	0.22325
130.0	1.91309	0.22736
150.0	1.89217	0.2317
170.0	1.87115	0.23628
190.0	1.85005	0.24112
210.0	1.82887	0.24623
230.0	1.80761	0.25165
250.8	1.78628	0.25738

The simulation results using the two boundary conditions are shown in Fig. 3a and Fig. 3b respectively. We can see that there is an obvious difference in pressure and saturation distributions. The results demonstrate that the flow direction has a big impact on the flow pattern. Therefore, we can point it out that the small-scale flow response inside a coarse-scale grid-block holding complex fracture structure could be heavily influenced by the local boundary condition. Furthermore, we can conclude that considering the effect of local boundary condition on the complex local-scale flow response is necessary for fractured reservoir simulation.

2.3. Multi-level discrete fracture model

In this section, assisted with a synthetic fracture network, we give a detailed description of the MLDFM implementation. We will construct two levels of the grid and split the whole fracture domain into many subdomains. In each subdomain, we apply the basis functions described in section 2.3.3 to determine the local boundary conditions at a fine scale. Based on that, we use the local upscaling method that is described in section 2.3.4 to recompute the transmissibility in a triple continuum model which is finally applied for forward simulation at a coarse scale.

2.3.1. Construct two levels of grid

We construct two levels of grid where the coarse-scale grid is applied for forward simulation and the fine grid is used to capture the fine-scale flow response. To guarantee an efficient and accurate simulation, the structured grid is employed on the coarse scale because of its flexibility when an unstructured grid is used on the fine scale to represent all fractures explicitly. In this study, these two grids are required to conform with each other for the convenience of the following implementations.

Taking a synthetic fracture network shown in Fig. 1 as an example, we first mesh it with a structured grid shown in Fig. 4. Then, we generate a fine unstructured grid using Gmsh (Geuzaine and Remacle, 2009) shown in Fig. 5. Out of the purpose of a better visualization, the domain is only part of Fig. 4.

Thanks to the explicit representation of all fractures in fine grid, the small-scale flow response could be accurately captured with the DFM. Assisted with upscaling of the fine-scale solutions, we could construct a triple continuum model on the coarse structured grid for forward simulation where the large-scale fractures are represented with numerical EDFM and the small-scale fractures are upscaled as a third continuum.

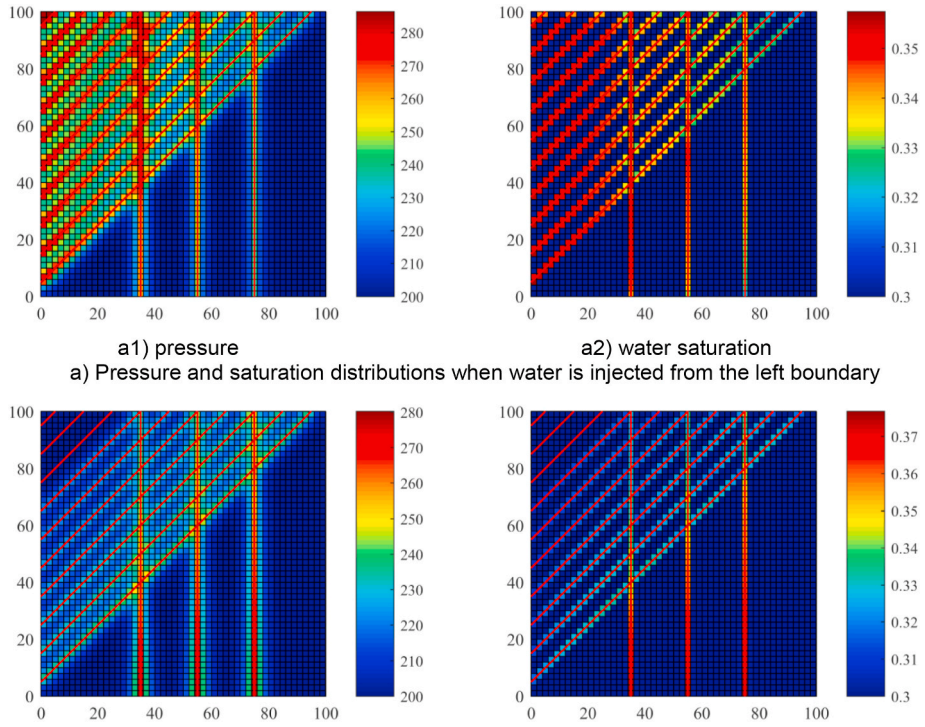

Fig. 3. The effect of flow direction on the flow response in a local fractured domain. We inject water at the left or bottom side of the fracture network with constant bottom hole pressure. a) Pressure and saturation distributions when water is injected from the left boundary, b) Pressure and saturation distributions when water is injected from the bottom boundary.

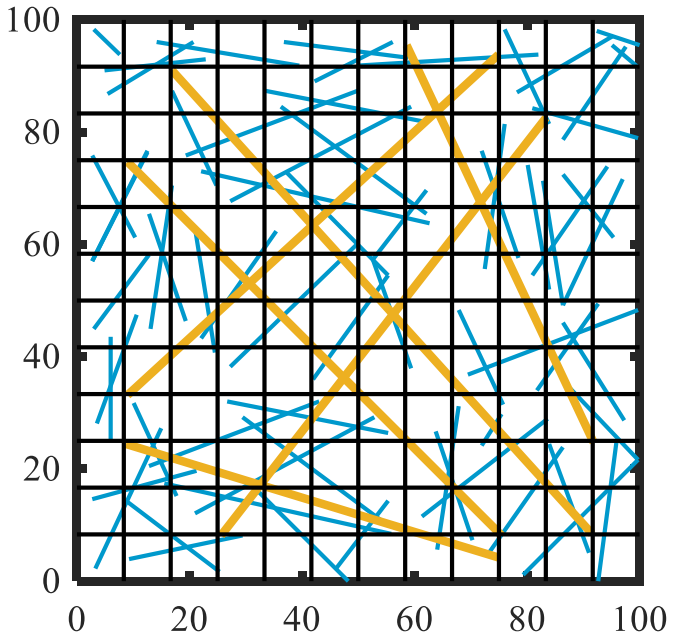

Fig. 4. Structured gridding on the coarse scale. Black thick lines are boundaries of the reservoir, blue lines represent small-scale fractures, yellow lines represent large-scale fractures, black thin lines represent the boundaries of coarse grid-blocks. (For interpretation of the references to colour in this figure legend, the reader is referred to the Web version of this article.)

However, due to the large gridblocks number, it is challenging to directly predict flow response based on the solution of fine scale model. To resolve that, we apply the local upscaling technique. Next, we will describe how to construct a subdomain for the local upscaling.

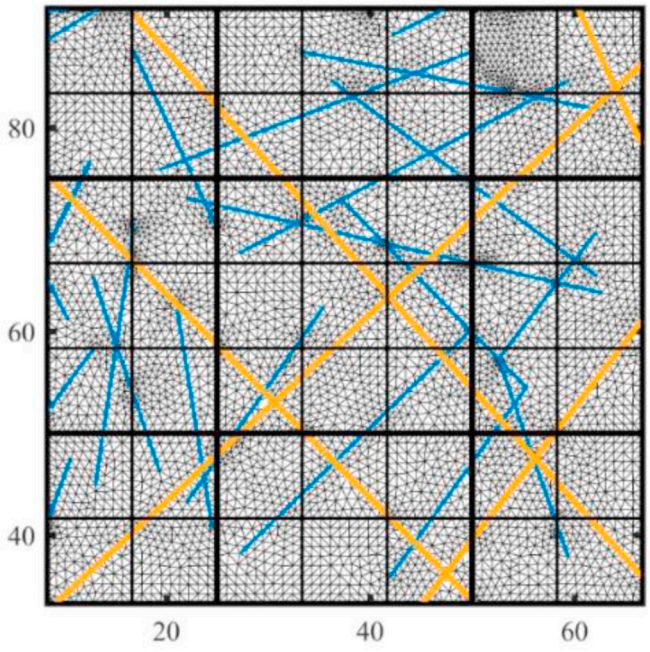

Fig. 5. Unstructured gridding on the fine scale. This is a local region of the whole domain; the coordinates help to determine its position in Fig. 4; the large-scale fractures in yellow and small-scale fractures in blue are represented explicitly; the unstructured grid is conformal with the boundary lines of coarse grid-blocks. (For interpretation of the references to colour in this figure legend, the reader is referred to the Web version of this article.)

2.3.2. *Construct subdomains*

As discussed in literatures (Gomez-Hernandez and Wen, 1994; Holden and Lia, 1992), an extended domain helps to improve the

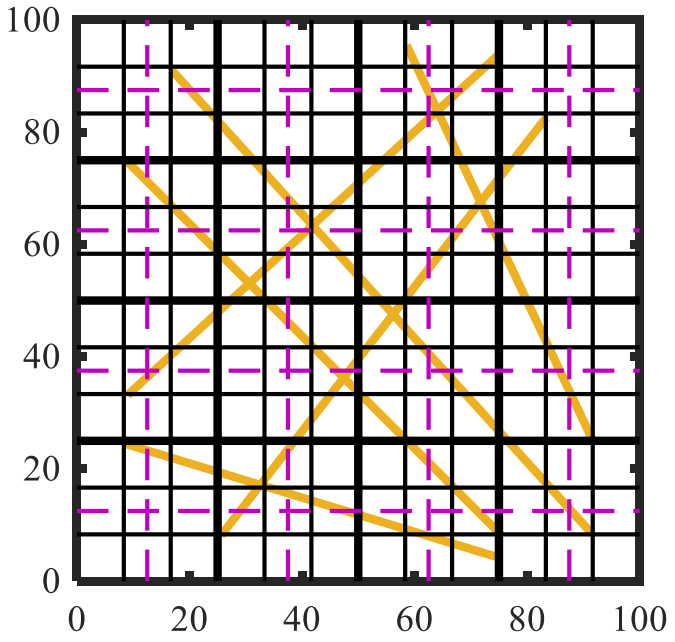

Fig. 6. Generate extended subdomains. Black thick lines are the boundaries of subdomains; black thin lines represent the boundaries of coarse grid-blocks; each subdomain contains 3 × 3 coarse grid-blocks; an extended subdomain is larger than a subdomain and is composed of four regions where each region is enclosed by the purple lines. (For interpretation of the references to colour in this figure legend, the reader is referred to the Web version of this article.)

accuracy of upscaled solution in the local upscaling. Therefore, we apply the extended local upscaling in this work. First, we split the original model by many subdomains as shown in Fig. 6. Each subdomain contains 3 × 3 coarse grid-blocks. Based on that, we determine extended subdomains also shown in Fig. 6. For a better understanding, we display an extended subdomain containing 7 × 7 coarse grid-blocks in Fig. 7. Next, we describe how to determine the boundary conditions in this extended subdomain.

2.3.3. Basis functions for the local boundary condition

For a typical extended local upscaling, the boundary conditions that apply constant pressure boundaries on the left and right sides and employ no-flow boundaries on up and bottom sides are used to estimate the k_x. But due to the existence of complex fracture networks, the flow response inside the extended subdomain could be heavily affected by the fracture distributions and thus influenced by the flow direction. Therefore, the typical approach may fail to provide accurate upscaled solution. Moreover, the fine grid in this study is unstructured which is also different from the typical extended local upscaling.

In this work, we derive local boundary conditions from the global pressure solution that is obtained by solving the coarse-scale triple continuum model to account for the effect of flow directions on the local flow response. Thanks to that, an adaptive and accurate local boundary condition can be resolved. Below is the detailed procedure using the finite-volume basis functions (Hajibeygi et al., 2011; Wang et al., 2014; Ţene et al., 2015).

First, we determine the boundary lines which are drawn in purple and yellow in Fig. 7. Note that the yellow lines represent large fractures. Second, we determine all the fine unstructured cells around the purple lines and the elements on the yellow lines. Here, we call them as boundary control volumes. Third, among all the boundary control volumes, we select the gridblocks located at the matrix and fracture coarse nodes as shown in Fig. 7. Here, we call them as basis control volumes.

Fourth, according to the number of matrix coarse nodes and fracture coarse nodes shown in Fig. 8, we perform local steady-state simulations on the boundary control volumes. In each simulation, we force the pressure of basis control volume at one coarse node as 1 and the pressure of the other basis control volumes as 0. The pressure values of boundary control volumes form the basis functions. For example, as shown in Fig. 9a, we set pressure of basis control volume at matrix coarse node i (in red) equal to 1 and pressure of other basis control volumes equal to 0. The pressure value of a matrix control volume j is taken as Φ_{ij}^{mm}, while the pressure value of fracture control volume j is taken as Φ_{ij}^{mf}. With a similar approach, we set the pressure of basis control volume on fracture coarse node i (in red in Fig. 9b) equal to 1 and pressure of other basis control volumes equal to 0 and determine Φ_{ij}^{fm} and Φ_{ij}^{ff}.

Finally, since we know the pressure values on the coarse nodes from global solution, we can compute the pressure values of boundary control volumes applying the basis function. The pressure value of matrix control volume j can be computed by Eq. (6).

$$P_j^m = \sum_{i=1}^{N_{cm}} \Phi_{ij}^{mm} P_i^m + \sum_{i=1}^{N_{cf}} \Phi_{ij}^{fm} P_i^f \tag{6}$$

The pressure value of fracture control volume j can be computed by Eq. (7).

$$P_j^f = \sum_{i=1}^{N_{cm}} \Phi_{ij}^{mf} P_i^m + \sum_{i=1}^{N_{cf}} \Phi_{ij}^{ff} P_i^f \tag{7}$$

Here, N_{cm} is the number of matrix coarse nodes; N_{cf} is the number of fracture coarse nodes; subscripts m and f represent matrix and fractured porous media. P_i^m and P_i^f are taken from global solution.

Note that at the beginning of the simulation, the pressure distributes uniformly in coarse scale without any difference. For this situation, we apply the typical extended local upscaling.

2.3.4. Local upscaling

Knowing the local boundary condition for an extended subdomain,

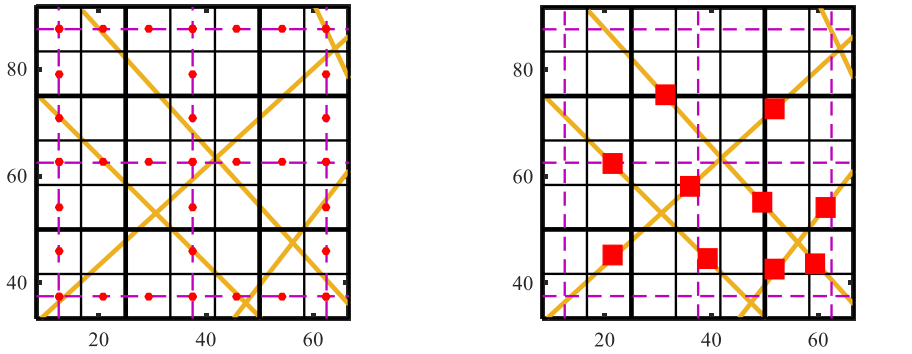

Fig. 7. The boundary lines and coarse nodes in an extended subdomain. The purples lines represent boundary lines; the large-scale fractures in yellow are also taken as boundary lines; the matrix coarse nodes are represented with red point; the fracture coarse nodes are represented with red squares. This extended subdomain contains 7 × 7 coarse grid-blocks; the coordinates help to determine its position in Fig. 6. (For interpretation of the references to colour in this figure legend, the reader is referred to the Web version of this article.)

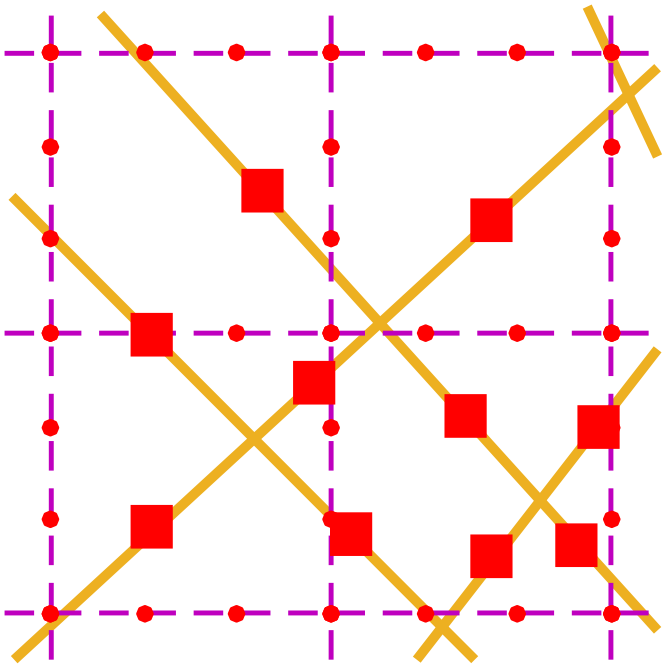

Fig. 8. Local boundary lines and coarse nodes. The lines in purple and yellow represent boundary lines; the red points on the purple lines and red squares on the yellow lines represent the coarse nodes; we know the pressure values on coarse nodes from global solution. The purple lines, yellow lines, red points, and red squares are taken from Fig. 7. (For interpretation of the references to colour in this figure legend, the reader is referred to the Web version of this article.)

we can perform a local steady-state simulation on the fine unstructured grid to reproduce the small-scale flow response. Based on this solution, we re-compute the transmissibility among matrix, large fractures, and small fractures using a single-phase flow-based numerical upscaling (Durlofsky et al., 2012).

The governing equation for steady-state simulation in the local region can be written as below:

$$\nabla \cdot \left(-k^f \nabla p^f\right) = 0 \tag{8}$$

Here, superscript f means fine scale. The flux between two neighboring fine control volumes is defined as:

$$\left(q^f\right)_l = \left(T^f \Delta p^f\right)_l \tag{9}$$

where q represents flux; T represents the transmissibility.

The flux between two neighboring coarse control volumes can be written as below:

$$q^c = \sum_l \left(q^f\right)_l \tag{10}$$

where superscript c means the coarse scale; l represents all the fine scale interfaces on a coarse scale interface. The pressure of coarse control volumes can be obtained using the volume-average method:

$$p_m^c = \langle p^f \rangle_m \qquad p_n^c = \langle p^f \rangle_n \tag{11}$$

where subscripts m and n represent two neighboring coarse control volumes; $<\bullet>_m$ denotes a bulk-volume-averaged property computed over the fine control volumes which fall inside the coarse control volume m. Then the transmissibility between control volumes m and n can be written as:

$$T_{m,n}^c = \frac{q^c}{\left|p_m^c - p_n^c\right|} \tag{12}$$

Note that the transmissibility between matrix control volumes and that between large fracture elements are still computed by traditional discretization approach. Using an upscaling approach to update these transmissibilities could remove the limitation that requires the two grids to be conformal and thus simplify the pre-processing work in terms of grid generation. But since it may affect the accuracy of transmissibility computation, we are going to investigate the feasibility of such an approach in our future work.

2.4. Adaptive local-global upscaling

Due to the adjustment of field development plan and the variety of multi-scale heterogeneities, the local boundary conditions are not static during a simulation run. Moreover, as discussed in (Renard and de

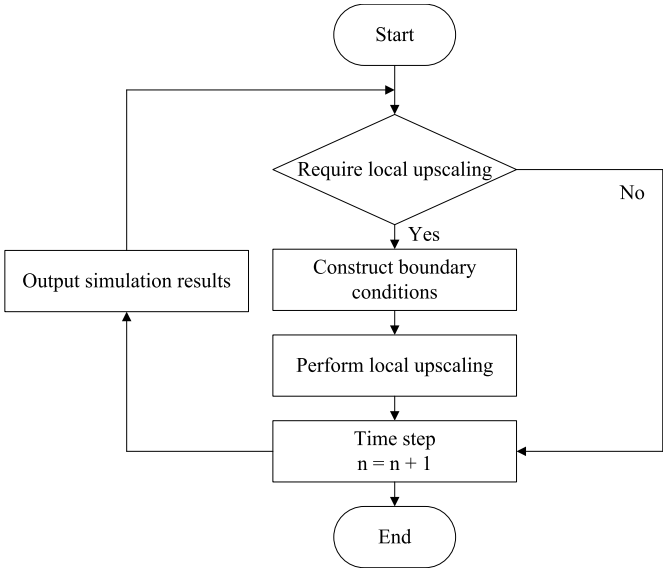

Fig. 10. Implementation procedure of adaptive local-global upscaling.

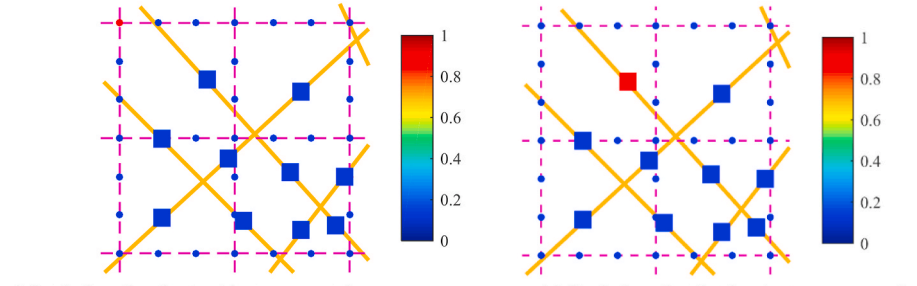

a) Basis function for matrix coarse node

b) Basis function for fracture coarse node

Fig. 9. Schematic of computing basis function. We perform many steady-state simulations on the boundary control volumes which are near purple lines and on the yellow lines to determine basis functions. For example, in figure a, we force the pressure value of the fine control volume at the red coarse node as 1, and force the pressure values of the fine control volumes at the blue coarse nodes and blue squares as 0. The pressure values of boundary control volumes form the basis function. (For interpretation of the references to colour in this figure legend, the reader is referred to the Web version of this article.)

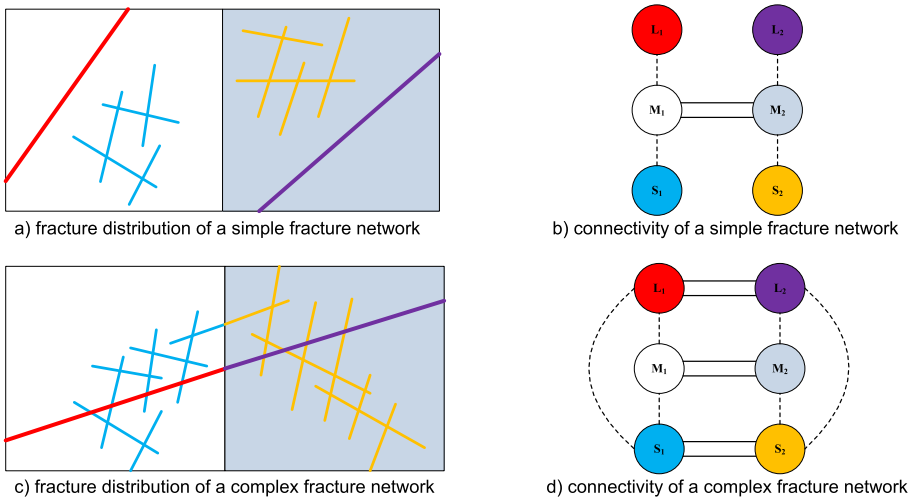

Fig. 11. The fracture distribution and corresponding connectivity between continuums. Here, we only show two types of fracture network for illustration, one is simple and the other is complex. M_1 represents the white grid-block; M_2 represents the light blue grid-block; L_1 represents the large fracture in red in the white grid-block; L_2 represents the large fracture in purple in the light blue grid-block; S_1 represents the small fractures in blue in the white grid-block; S_2 represents the small fractures in yellow in the light blue grid-block. (For interpretation of the references to colour in this figure legend, the reader is referred to the Web version of this article.)

Marsily, 1997; Miller et al., 1998), the changes in boundary conditions have a large effect on local upscaling solutions. Therefore, we perform the local upscaling adaptively following the local-global upscaling procedure (Chen et al., 2003; Li and Durlofsky, 2016). In this way, dynamic and accurate boundary conditions can be guaranteed for local upscaling. The flow chart of the implementation procedure is described in Fig. 10. We describe the details as follows.

First, according to the current simulation time, we determine whether to perform the local upscaling or not. If yes, we perform the local upscaling. If not, we continue the forward simulation. Second, if local upscaling is necessary, we determine the local boundary conditions following section 2.3.3. Third, we perform local upscaling to update the transmissibility for coarse-scale forward simulation. The way to compute the transmissibility is described in Eqs. (13)–(16).

$$T^c_{M_m,S_n} = \frac{q^c_{M_m,S_n}}{|p^c_{M_m} - p^c_{S_n}|} \tag{13}$$

$$T^c_{M_m,L_n} = \frac{q^c_{M_m,L_n}}{|p^c_{M_m} - p^c_{L_n}|} \tag{14}$$

$$T^c_{S_m,S_n} = \frac{q^c_{S_m,S_n}}{|p^c_{S_m} - p^c_{S_n}|} \tag{15}$$

$$T^c_{S_m,L_n} = \frac{q^c_{S_m,L_n}}{|p^c_{S_m} - p^c_{L_n}|} \tag{16}$$

Here the superscript c represents coarse scale; the subscripts M, S, and L represent matrix, small fractures, and large fractures porous media; the subscripts m and n represent two neighboring coarse control volumes. Note that the small fractures that fall inside the same coarse structured grid are upscaled as a single continuum. As a result, we obtain a triple continuum model for the coarse-scale forward simulation where large fractures are represented with numerical EDFM and small fractures are upscaled as a third continuum. It is important to mention that the DFM technique has already reached certain maturity in representation of 2D and 3D fractured networks (Berre et al., 2021). However, an application of DFM to realistic fractured networks with several thousand fractures (e.g. based on outcrop interpretation) is still a challenging problem due to the high complexity of meshing. The EDFM approach is a more suitable technique for this type of applications and this is where MLDFM can significantly improve the accuracy of approximation. Considering the fact that there are limited number of fractures in each subdomain, we apply the DFM, which provides better solutions than that of EDFM but requires an unstructured grid, to accurately reproduce the fine-scale complex flow response.

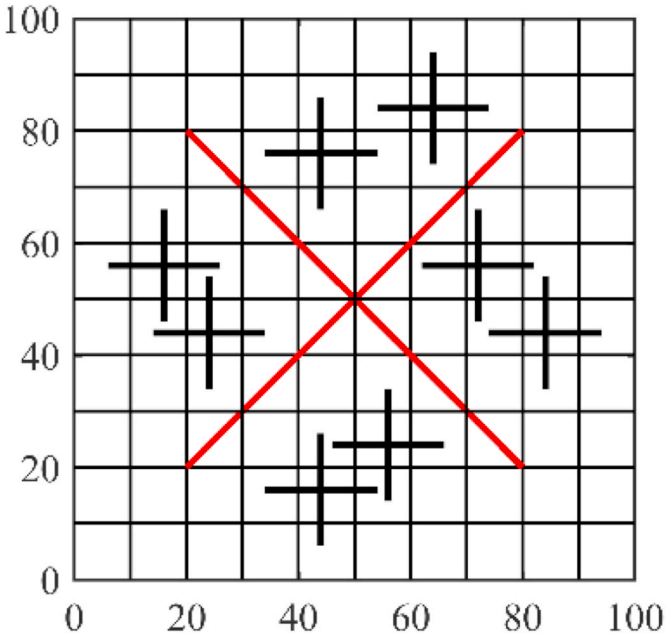

Fig. 12. The schematic of a simple fracture network. Red thick lines represent large-scale fractures, black thick lines represent small-scale fractures, black thin lines represent the boundaries of coarse grid-blocks. (For interpretation of the references to colour in this figure legend, the reader is referred to the Web version of this article.)

To display the triple continuum model in an intuitive way, we show the connectivity between the continuums in Fig. 11. Since the fractures may vary in a wide range of length scales in realistic fractured reservoirs, we are going to extend the fracture network from two levels presented in this study to three or more levels in future research. A new triple continuum model will be introduced where the large-scale fractures are represented with numerical EDFM, the middle-scale fractures are represented with a third continuum, and the small-scale fractures are homogenized into the matrix.

3. Numerical results

In this section, we present several tests to demonstrate the performance of the MLDFM. First, we benchmark the MLDFM solution with the fine DFM and traditional EDFM solutions. Next, we study with several examples the sensitivity of the MLDFM solutions to different

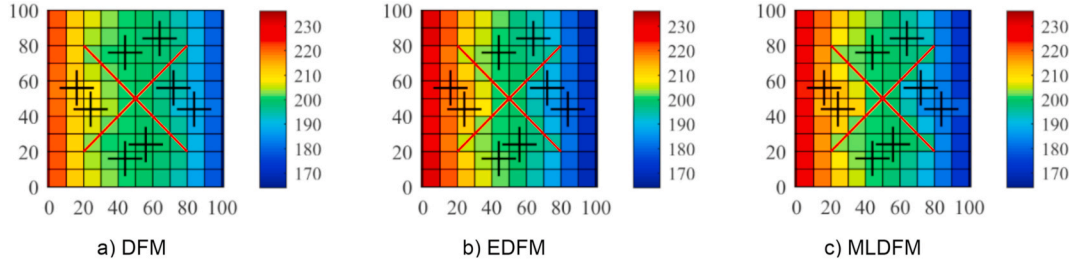

Fig. 13. The pressure distributions obtained from DFM, conventional EDFM and MLDFM (injected PV = 0.01). The solutions are shown on the coarse grid; the solution of DFM is obtained by volume weighted method. The fine unstructured grid used for DFM and MLDFM is not shown here. Since the length of all fractures is larger than the size of the coarse-scale grid-block, we represent all fractures with numerical EDFM in MLDFM. To constrain boundary condition, we attach skin grid-blocks that have tiny volume and very high permeability on the left and right boundaries of the domain. The dimension of the grid-blocks is 12 × 10. This test shows the accuracy and feasibility of numerical EDFM in MLDFM.

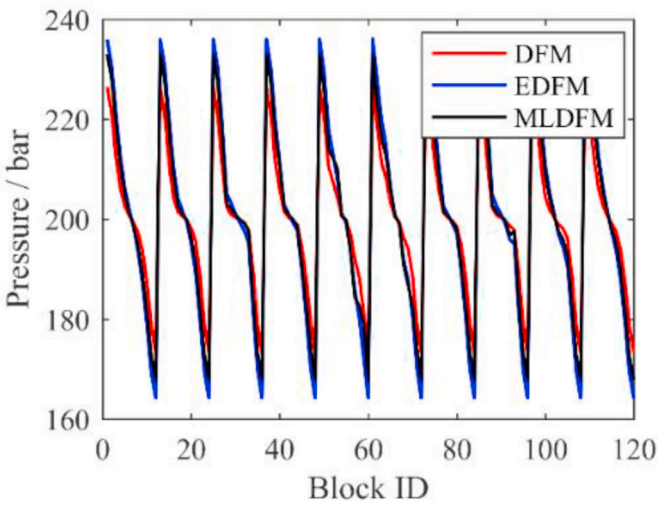

Fig. 14. The comparison of pressure solutions obtained from DFM, conventional EDFM and MLDFM (injected PV = 0.01). Since we attach skin grid-blocks on the left and right boundaries of the domain, the number of grid-blocks is 120. If a grid-block is numbered as J and I in x and y directions respectively, the block ID of this grid-block is (I-1) × 12 + J. The block ID of the left bottom grid-block is 1, the block ID of the right up grid-block is 120.

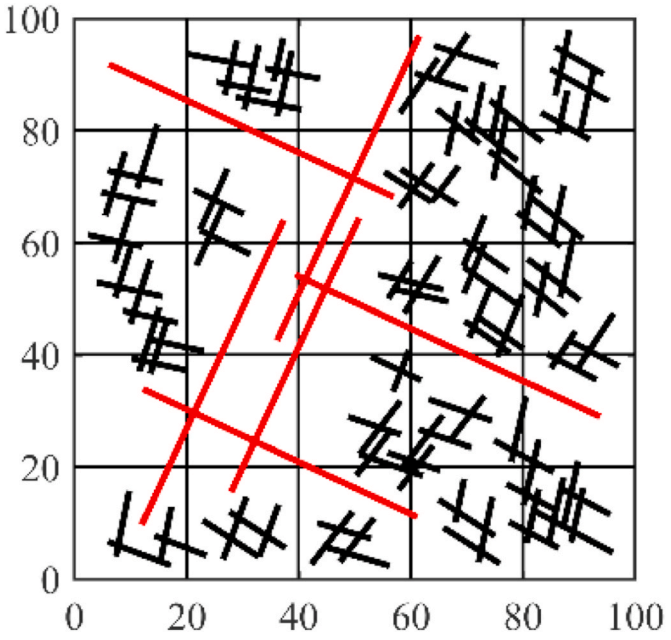

Fig. 15. The schematic of a complex fracture network. Red thick lines represent large-scale fractures, black thick lines represent small-scale fractures, black thin lines represent the boundaries of coarse grid-blocks. (For interpretation of the references to colour in this figure legend, the reader is referred to the Web version of this article.)

boundary conditions and the type of small features. Finally, we investigate the feasibility of the MLDFM method for realistic fractured reservoirs.

3.1. Simple fracture network

In this case, using a simple fracture network in Fig. 12, we benchmark the numerical solutions of MLDFM and EDFM with a reference solution, obtained using a high-resolution DFM. The EDFM solution is obtained by solving the traditional EDFM model, see (Hajibeygi et al., 2011; Tene et al., 2017) for details regarding the computation of fracture-matrix transmissibility. The reference solution is based on a conforming grid that is fully converged numerically, see (Sartori, 2018) for details. The reservoir is saturated with water, the properties of reservoir and fluid are taken from Tables 1 and 2 The upper and lower boundaries are impermeable, the left and right boundaries are imposed with constant injection and production rates equaling to 200 Kg/day. The injected pore volume is 0.01.

Since the length of all fractures is larger than the size of the coarse-scale grid-block, we represent all fractures with numerical EDFM in MLDFM. From Fig. 13, we can see that the three solutions of DFM, EDFM, and MLDFM are very similar. The results demonstrate the accuracy and feasibility of the numerical EDFM in MLDFM. Moreover, we compare the pressure solutions in Fig. 14. By averaging the fine DFM solution to the coarse grid and taking it as a reference, the relative errors (defined by Eq. (17)) of the conventional EDFM and MLDFM are equal to 3.06% and 2.04% respectively. The pressure error in MLDFM is 1.5 times lower than in conventional EDFM.

$$err = \sum_{i=1}^{NB} \frac{|p_{MLDFM,i} - p_{DFM,i}|}{p_{DFM,i}} \Big/ NB \tag{17}$$

where *NB* is the number of coarse matrix grid-blocks. This error is applied for all examples in this paper.

In this test, the results prove that the MLDFM is capable to provide slightly more accurate solutions than the EDFM when all the fractures have a length in the same order as the grid-block size or much longer. Next, we will test a fracture network with shorter fractures compared with grid-block size.

3.2. Complex fracture network

In this section, we investigate the performance of the MLDFM in

Table 4
Relative permeability (Corey equation).

Parameter	Value
Phase exponent	2
Oil exponent	4
Irreducible phase saturation	0
Residual oil saturation	0
End point of the oil relative permeability curve	1

Table 5
Injection/Production strategy.

Parameter	Value	Unit
Injection rate	500	kg/d
Production rate	500	kg/d
Injected pore volume	0.25	

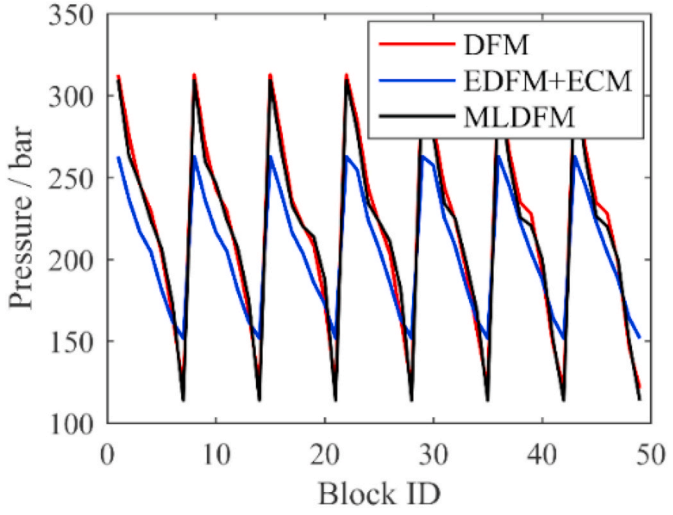

Fig. 16. The pressure distributions (injected PV = 0.25). If a grid-block is numbered as J and I in x and y directions respectively, the block ID of this grid-block is (I-1) × 7 + J. The block ID of the left bottom grid-block is 1, the block ID of the right up grid-block is 49. The numbering approach of block ID is used in the following figures.

multiphase flow using a more complex fractured model shown in Fig. 15. The boundary condition is the same as that applied in the previous example. The reservoir, fluid, and boundary condition parameters are taken from Table 1 through 5. Since the length of small-scale fractures is much smaller than the grid-block size, we apply the idea of the hierarchical fracture model (HFM) in the comparison instead of EDFM. Here, the large-scale fractures are represented with the traditional EDFM when the small-scale fractures are homogenized into matrix using upscaling method. See the treatment of type III fractures in (Guo et al., 2019) for the details of the upscaling method. In this work, we refer to it as EDFM + ECM where ECM represents Equivalent Continuum Model. Besides, the small-scale fractures are upscaled as a third continuum in the MLDFM.

We compare the solutions of MLDFM and EDFM + ECM with the high-resolution DFM solution. As shown in Figs. 16 and 17, the fracture network introduces a complex multi-scale flow response which affects multiphase transport in all models. The pressure solutions, shown in Fig. 16, demonstrate that MLDFM provides a better solution in comparison to the EDFM + ECM. Taking the fine DFM solution as a reference, the pressure errors of the EDFM + ECM and MLDFM are equal to 11.60% and 3.29% respectively. In addition, the saturation distributions, shown in Fig. 17, demonstrate that MLDFM could predict the main flow path more accurately than EDFM + ECM. The saturation errors of the EDFM + ECM and MLDFM are equal to 13.35% and 6.45% respectively. Notice that the pressure error in MLDFM is almost 4 times lower than that in EDFM + ECM when both models are applied to multiphase flow in the complex fracture network. The improvement of the simulation accuracy in MLDFM is achieved by an application of the triple continuum model in a dynamic manner which enhances the modelling capabilities by considering the effect of a local flow redistribution at subscale of EDFM.

3.3. Sensitivity analysis

In this section, we will demonstrate the robustness of MLDFM through sensitivity analysis.

3.3.1. Sensitivity to the flow boundary condition

As shown above, boundary conditions play a vital role in flow response. In this section, by using the fracture network in Fig. 15, we investigate the sensitivity of all three model solutions to boundary conditions. The reservoir, fluid, and boundary condition parameters are taken again from Table 1 through 5. We design three flow directions shown in Fig. 18. Since the solution for the first boundary condition is already obtained in the last section and shown in Figs. 16 and 17, we only run simulations for the second and third boundary conditions here. The pressure solutions, shown in Fig. 19, demonstrate that the MLDFM is capable to provide significantly better solutions than the EDFM + ECM at different boundary conditions. The saturation distributions, shown in Figs. 20 and 21, demonstrate that MLDFM could predict the main flow path more accurately than EDFM + ECM. The errors are shown in Table 6.

3.3.2. Sensitivity to the type of small features

The type of small features also has significant impact on the flow response. While the large-scale fractures control the major flow distribution, the small-scale fractures affect it at the local scale. In this section, we investigate the sensitivity of solutions of the three models to the type of small-scale fractures. To reach this goal, we generate a new geological

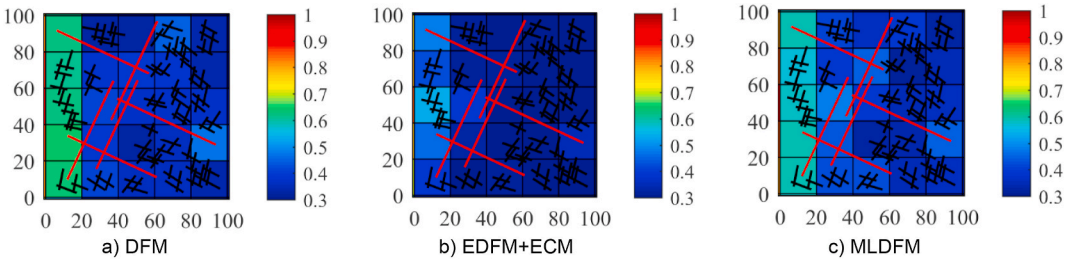

Fig. 17. The water saturation distributions (injected PV = 0.25). To constrain boundary condition, we attach skin grid-blocks that have tiny volume and very high permeability on the outer boundaries of the domain. The dimension of the grid-blocks is 7 × 7. What the way to attach skin grid-blocks is used in the following figures.

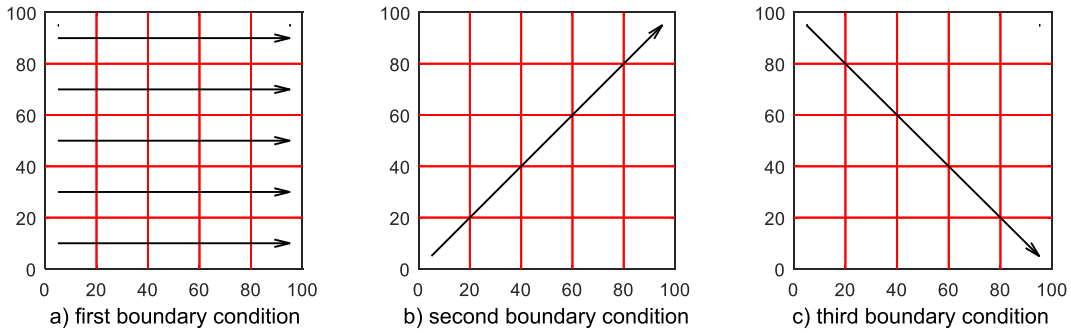

Fig. 18. The schematic of three flow conditions.

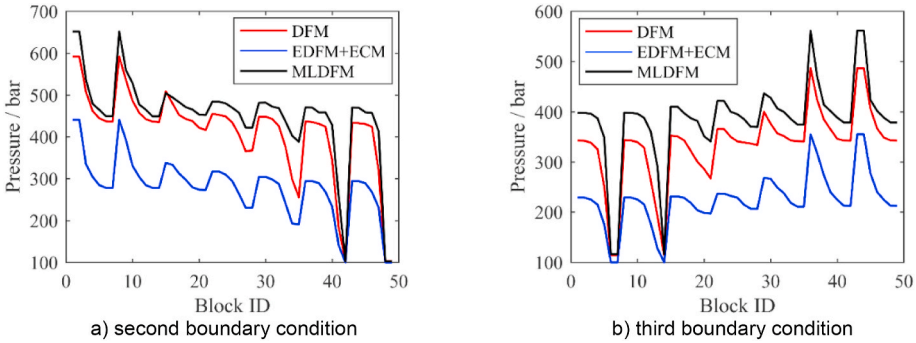

Fig. 19. The pressure distributions at the second and third type of global boundary conditions (injected PV = 0.25).

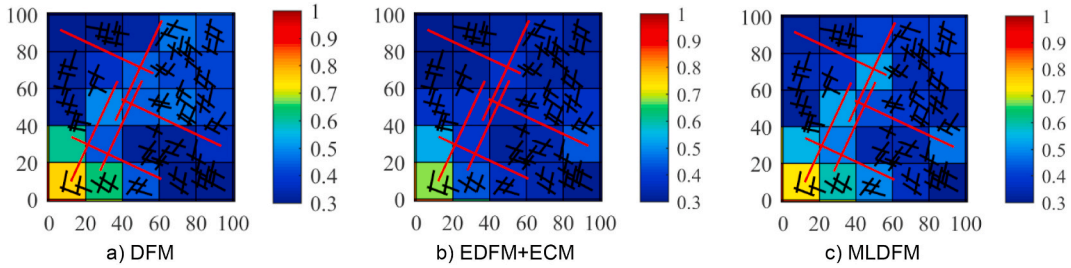

Fig. 20. The water saturation distributions at the second flow condition (injected PV = 0.25).

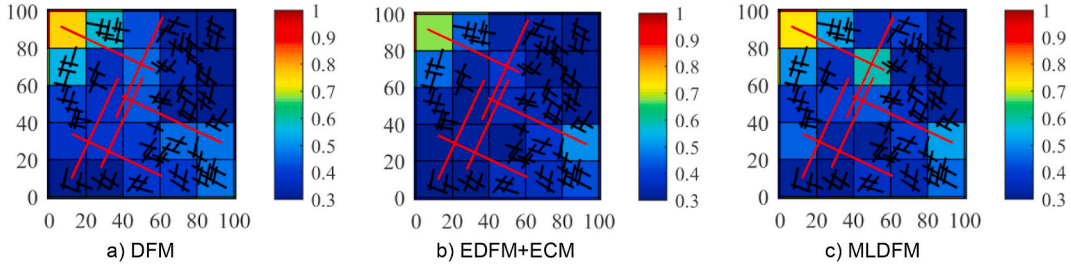

Fig. 21. The water saturation distributions at the third flow condition (injected PV = 0.25).

Table 6
Errors of EDFM + ECM and MLDFM compared with DFM at three boundary conditions.

Boundary conditions	Pressure error, %		Saturation error, %	
	EDFM + ECM	MLDFM	EDFM + ECM	MLDFM
Type 1	11.60	3.29	13.35	6.45
Type 2	30.74	9.87	10.36	8.22
Type 3	32.05	15.28	8.36	7.89

model by changing fracture connectivity of the fracture network in Fig. 15. As shown in Fig. 22, we removed most of the small-scale features of which the angles are larger than 90°. Again, the reservoir, fluid, and well condition parameters are taken from Table 1 through 5.

Pressure and saturation solutions are shown in Figs. 23 and 24 respectively. Taking the DFM solution as a reference, the pressure errors of the EDFM + ECM and MLDFM are equal to 15.66% and 2.96% respectively. The saturation errors of the EDFM + ECM and MLDFM are equal to 14.04% and 8.54% respectively. The results demonstrate again

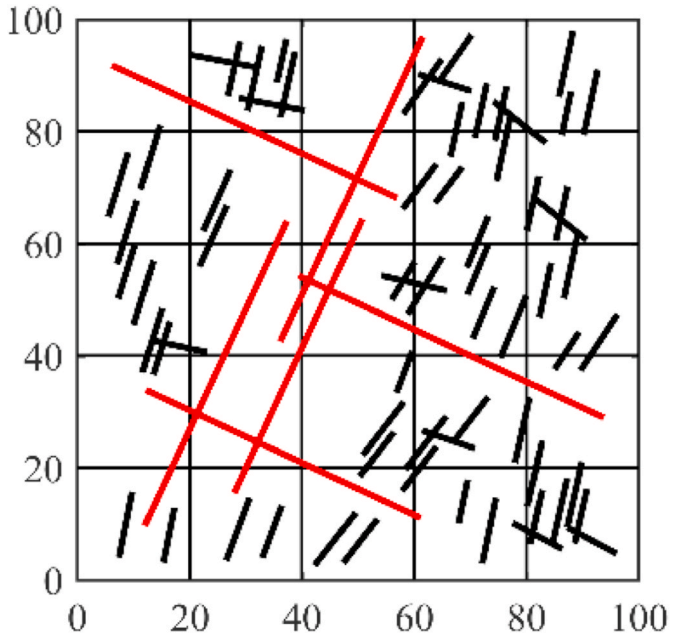

Fig. 22. The schematic of a modified fracture network. Remove most of the small-scale fractures of which the angles are larger than 90° from the fracture network shown in Fig. 15. Red thick lines represent large-scale fractures, black thick lines represent small-scale fractures, black thin lines represent the boundaries of coarse grid-blocks. (For interpretation of the references to colour in this figure legend, the reader is referred to the Web version of this article.)

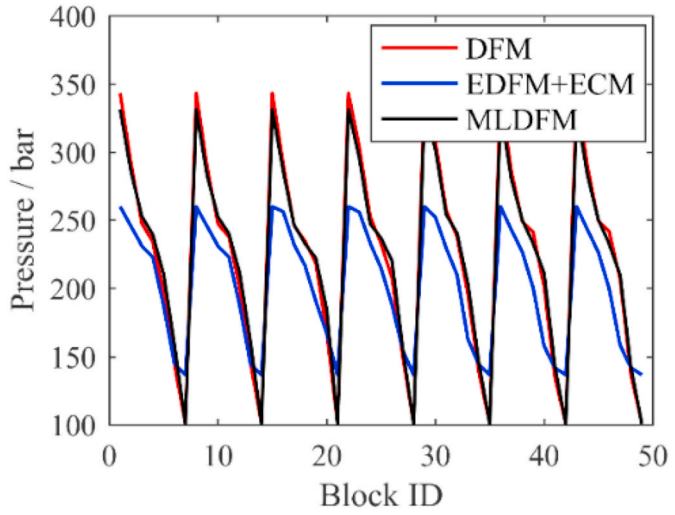

Fig. 23. The pressure distributions of the test using a modified fracture network (injected PV = 0.25). The first flow condition is applied.

that MLDFM could provide more accurate solutions than EDFM + ECM for different small features types.

3.4. Realistic fracture network

In this section, we test MLDFM with a complex fracture network from Apodi, Brazil (Bertotti and Bisdom, 2013; Bisdom et al., 2016) shown in Fig. 25. The reservoir dimension is 300 × 300 m, the first boundary condition shown in Fig. 18 is applied, the pressures at the left and right boundaries are fixed at 300 and 100 bar respectively, the injected pore volume of fine DFM model is 0.20, and other parameters are taken from Table 1 through 5.

The pressure and water saturation solutions obtained by DFM, EDFM + ECM, and MLDFM simulations are shown in Figs. 26 and 27. Taking the fine DFM solution as a reference, the pressure errors of the EDFM + ECM and MLDFM are equal to 4.40% and 2.39% respectively, the saturation errors of the EDFM + ECM and MLDFM are equal to 18.34% and 8.10% respectively. Besides, the error of saturation in MLDFM model is distributed more uniformly with a lower amplitude in comparison to EDFM + ECM approach where errors are near the main displacement front.

The results demonstrate that the MLDFM can provide more accurate solutions than EDFM + ECM for reservoirs simulations employing complex realistic fracture networks. The number of control volumes corresponding to DFM, EDFM + ECM, and MLDFM are 334,774, 998 and 1145 respectively. Compared with DFM, MLDFM saves about 97% simulation time and is comparable by performance with EDFM + ECM. Therefore, we can conclude that MLDFM is an accurate and computationally efficient forward-simulation method for complex naturally fractured reservoirs.

4. Conclusions

We present a multi-level discrete fracture model (MLDFM) for

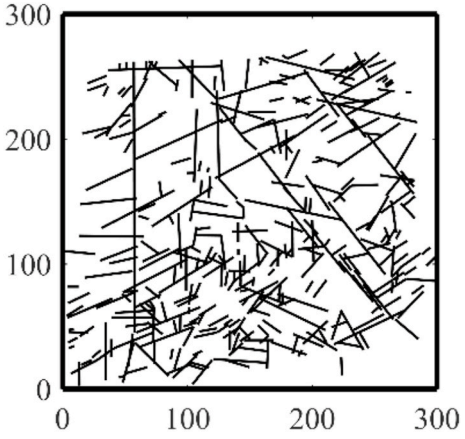

Fig. 25. A realistic fracture network from Apodi, Brazil.

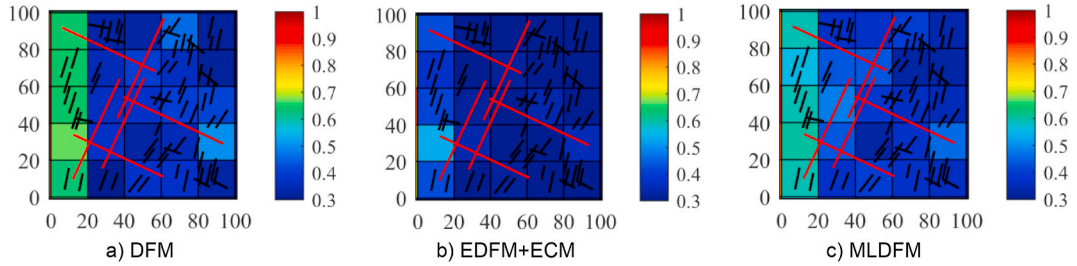

Fig. 24. The water saturation distributions of the test using a modified fracture network (injected PV = 0.25). The first flow condition is applied.

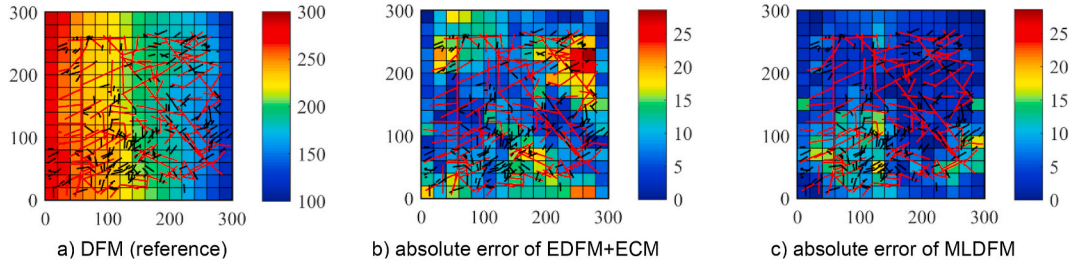

Fig. 26. The pressure distributions and the absolute errors of EDFM + ECM and MLDFM (injected PV = 0.20). The red thick lines represent large-scale fractures; the black thick lines represent small-scale fractures. In MLDFM, the large-scale fractures are represented with numerical EDFM when the small-scale fractures are upscaled as a third continuum. Absolute error of MLDFM = abs (p_DFM – p_MLDFM). To constrain boundary condition, we attach skin grid-blocks that have tiny volume and very high permeability on the outer boundaries of the domain. The dimension of the grid-blocks is 17 × 17. (For interpretation of the references to colour in this figure legend, the reader is referred to the Web version of this article.)

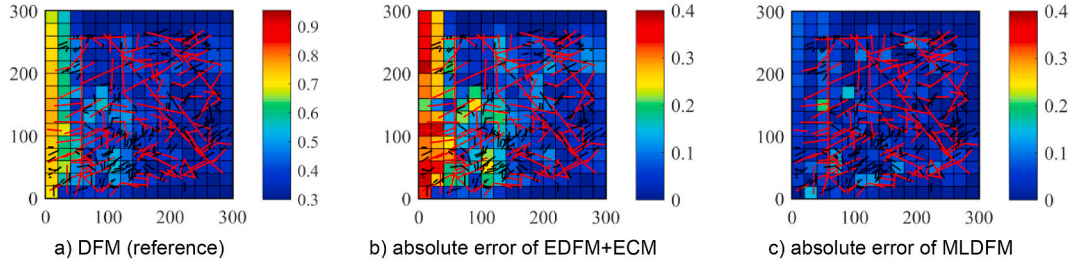

Fig. 27. The water saturation distributions and the absolute errors of EDFM + ECM and MLDFM (injected PV = 0.20).

naturally fractured reservoir simulation. To guarantee accurate and efficient solutions, we couple fine-scale solutions within a coarse-scale forward simulation.

In the coarse-scale forward simulation, we apply a triple continuum model on a structured grid where large fractures are approximated explicitly utilizing the numerical EDFM and the secondary features are upscaled as a third continuum. Different from the previous work, the numerical EDFM and the third continuum are treated in a dynamic manner considering the effect of changes in flow direction on the complex multi-scale flow response.

In the fine-scale simulation, we use DFM on an unstructured grid that approximates all fractures explicitly. Thanks to that, the small-scale flow response can be captured accurately.

For the convenience of implementation, the fine grid is conformal to the boundary of coarse grid. Benefit from that, it is easy to couple the upscaled solution of fine-scale simulation within the coarse-scale forward simulation.

To guarantee the robustness and accuracy of the upscaled solution, we apply the flow-based method for the extended local upscaling. Moreover, since the flow direction has a large effect on the upscaled solution, we derive local boundary conditions at fine scale from the global pressure solution employing basis functions. What improves the solution furthermore is that we apply a local-global upscaling formalism to ensure changes in local boundary conditions.

We present several numerical cases to demonstrate the performance of MLDFM. The test mimicking single-phase flow in a simple synthetic fracture network proves that the numerical EDFM approach in MLDFM is capable to improve the modelling capabilities of large-scale fractures. Moreover, we test several multi-phase flow cases using complex fracture networks. The results demonstrate that the MLDFM could also provide robust and accurate solutions for multi-phase flow modelling in complex fractured reservoirs. Besides, we test a multi-phase flow in a realistic fracture network based on outcrop observations. The results further demonstrate the feasibility and performance of MLDFM in applied field cases.

In view of the high modelling capabilities of DFM, we will present a hybrid model using DFM in both coarse-scale and fine-scale simulations. Moreover, we will investigate the feasibility of applying EDFM at two scale simulations which could significantly simplify the implementation of MLDFM. Besides, considering the realistic applications, we will apply the MLDFM to 3D problems.

Credits

Longlong Li: Methodology, Investigation, Software, Validation, Writing – original draft, Denis Voskov: Conceptualization, Methodology, Supervision, Writing – review & editing, Project administration

Declaration of competing interest

The authors declare that they have no known competing financial interests or personal relationships that could have appeared to influence the work reported in this paper.

Acknowledgment

We acknowledge the financial support of China Scholarship Council. We would also like to thank the Stanford University Petroleum Research Institute for Reservoir Simulation (SUPRI-B) program for the permission to use AD-GPRS in this work.

References

Awadalla, T., Voskov, D., 2018. Modeling of gas flow in confined formations at different scales. Fuel 234, 1354–1366. https://doi.org/10.1016/j.fuel.2018.08.008.

Barenblatt, G.I., Zheltov, Iu P., Kochina, I.N., 1960. Basic concepts in the theory of seepage of homogeneous liquids in fissured rocks. J. Appl. Math. Mech. 24 (5), 1286–1303. https://doi.org/10.1016/0021-8928(60)90107-6.

Berre, I., Doster, F., Keilegavlen, E., 2019. Flow in fractured porous media: a review of conceptual models and discretization approaches. In: Transport in Porous Media, vol. 130, pp. 215–236.

Berre, I., Boon, W.M., Flemisch, B., et al., 2021. Verification benchmarks for single-phase flow in three-dimensional fractured porous media. Adv. Water Resour. 147 https://doi.org/10.1016/j.advwatres.2020.103759.

Bertotti, G., Bisdom, K., 2013. Fracture patterns in the Jandeira Fm. (NE Brazil). http://data.4tu.nl/repository/uuid:be07fe95-417c-44e9-8c6a-d13f186abfbb.

Bisdom, K., Bertotti, G., Nick, H., 2016. The impact of different aperture distribution models and critical stress criteria on equivalent permeability in fractured rocks. J. Geograph. Res.: Solid Earth 121 (5), 4045–4063. https://doi.org/10.1002/2015JB012657.

Blaskovich, F.T., Cain, G.M., Sonier, F., et al., 1983. A Multicomponent Isothermal System for Efficient Reservoir Simulation. SPE 11480-MS.

Bourbiaux, B., 2010. Fractured reservoir simulation: a challenging and rewarding issue. Oil & Gas Sci. Technol. — Rev. IFP 65 (2), 227–238.

Chen, Y., Durlofsky, L.J., Gerritsen, M., et al., 2003. A coupled local-global upscaling approach for simulating flow in highly heterogeneous formations. Adv. Water Resour. 26 (10), 1041–1060. https://doi.org/10.1016/S0309-1708(03)00101-5.

Ding, D.Y., Farah, N., Bourbiaux, B., Wu, Y.-S., Mestiri, I., 2018. Simulation of Matrix/Fracture Interaction in Low-Permeability Fractured Unconventional Reservoirs. SPE 182608-PA.

Durlofsky, L.J., Chen, Y., 2012. Uncertainty quantification for subsurface flow problems using coarse-scale models. In: Graham, I., Hou, T., Lakkis, O., Scheichl, R. (Eds.), Numerical Analysis of Multiscale Problems. Lecture Notes in Computational Science and Engineering, vol. 83. Springer, Berlin, Heidelberg.

Fumagalli, A., Pasquale, L., Zonca, S., Micheletti, S., 2016. An upscaling procedure for fractured reservoirs with embedded grids. Water Resour. Res. 52 (8), 6506–6525.

Gallyamov, E., Garipov, T., Voskov, D., et al., 2018. Discrete fracture model for simulating waterflooding processes under fracturing conditions. Int. J. Numer. Anal. Methods GeoMech. 42 (13), 1445–1470. https://doi.org/10.1002/nag.2797.

Garipov, T.T., Karimi-Fard, M., Tchelepi, H.A., 2016. Discrete fracture model for coupled flow and geomechanics. Comput. Geosci. 20 (1), 149–160. https://doi.org/10.1007/s10596-015-9554-z.

Garipov, T.T., Tomin, P., Rin, R., et al., 2018. Unified thermo-compositional-mechanical framework for reservoir simulation. Comput. Geosci. 22 (4), 1039–1057. https://doi.org/10.1007/s10596-018-9737-5.

Gerke, H.H., van Genuchten, M.T., 1993a. A dual-porosity model for simulating the preferential movement of water and solutes in structured porous media. Water Resour. Res. 29 (2), 305–319. https://doi.org/10.1029/92WR02339.

Gerke, H.H., van Genuchten, M.T., 1993b. Evaluation of a first-order water transfer term for variably saturated dual-porosity flow models. Water Resour. Res. 29 (4), 1225–1238. https://doi.org/10.1029/92WR02467.

Geuzaine, C., Remacle, J.F., 2009. Gmsh: a 3-D finite element mesh generator with built-in pre- and post-processing facilities. Int. J. Numer. Methods Eng. 79 (11), 1309–1331. https://doi.org/10.1002/nme.2579.

Gomez-Hernandez, J.J., Wen, X.H., 1994. Probabilistic assessment of travel times in groundwater modeling. J. Stochas. Hydrol. Hydraul. 8 (1), 19–56.

Gong, B., 2007. Effective Models of Fractured Systems. PhD Dissertation. Stanford University, Stanford, California. September 2007.

Gong, J., Rossen, W.R., 2016. Shape factor for dual-permeability fractured reservoir simulation: effect of non-uniform flow in 2D fracture network. Fuel 184, 81–88.

Guo, Y., Liang, Y., Li, J., Gong, B., 2019. A novel connectivity-based hierarchical model for multi-scale fracture system in carbonate reservoir simulation. Fuel 250, 327–338.

Hajibeygi, H., Karvounis, D., Jenny, P., 2011. A hierarchical fracture model for the iterative multiscale finite volume method. J. Comput. Phys. 230 (24), 8729–8743. https://doi.org/10.1016/j.jcp.2011.08.021.

Holden, L., Lia, O., 1992. A tensor estimator for the homogenization of absolute permeability. Transport Porous Media 8, 37–46.

Hui, M.-H., Dufour, G., Vitel, S., et al., 2019. A Robust Embedded Discrete Fracture Modeling Workflow for Simulating Complex Processes in Field-Scale Fractured Reservoirs. SPE 193827-MS.

Jiang, J., Younis, R., 2016. Hybrid coupled discrete-fracture/matrix and multicontinuum models for unconventional-reservoir simulation. SPE J. 21 (3), 1–19, 0.

Karimi-Fard, M., Durlofsky, L.J., 2012. Accurate resolution of near-well effects in upscaled models using flow-based unstructured local grid refinement. SPE J. 17 (4), 1084–1095. https://doi.org/10.2118/141675-PA. SPE-141675-PA.

Karimi-Fard, M., Durlofsky, L.J., 2016. A general gridding, discretization, and coarsening methodology for modeling flow in porous formations with discrete geological features. Adv. Water Resour. 96, 354–372. https://doi.org/10.1016/j.advwatres.2016.07.019.

Karimi-Fard, M., Durlofsky, L.J., Aziz, K., 2004. An efficient discrete-fracture model applicable for general-purpose reservoir simulators. SPE J. 9 (2), 227–236. https://doi.org/10.2118/88812-PA. SPE-88812-PA.

Karimi-Fard, M., Gong, B., Durlofsky, L.J., 2006. Generation of coarse-scale continuum flow models from detailed fracture characterizations. Water Resour. Res. 42 (10), W10423. https://doi.org/10.1029/2006WR005015.

Lee, S.H., Jensen, C.L., Lough, M.F., 2000. Efficient finite-difference model for flow in a reservoir with multiple length-scale fractures. SPE J. 5 (3), 268–275. https://doi.org/10.2118/65095-PA. SPE-65095-PA.

Li, H., Durlofsky, L.J., 2016. Local-global upscaling for compositional subsurface flow simulation. Transport Porous Media 111 (3), 701–730. https://doi.org/10.1007/s11242-015-0621-7.

Li, L., Lee, S.H., 2008. Efficient field-scale simulation of black oil in a naturally fractured reservoir through discrete fracture networks and homogenized media. SPE Reservoir Eval. Eng. 11 (4), 750–758. https://doi.org/10.2118/103901-PA. SPE-103901-PA.

Liu, L., Huang, Z., Yao, J., Di, Y., Wu, Y., 2020. An Efficient Hybrid Model for 3D Complex Fractured Vuggy Reservoir Simulation. SPE 199899-PA.

Miller, C.T., Christakos, G., Imhoff, P.T., et al., 1998. Multiphase flow and transport modeling in heterogeneous porous media: challenges and approaches. Adv. Water Resour. 21 (2), 77–120. https://doi.org/10.1016/S0309-1708(96)00036-X.

Pruess, K., 1992. Brief Guide to the MINC-Method for Modeling Flow and Transport in Fractured Media. Tech. Rep. LBNL-32195. Lawrence Berkeley National Laboratory.

Pruess, K., Narasimhan, T.N., 1982. On fluid reserves and the production of superheated steam from fractured, vapor-dominated geothermal reservoirs. J. Geophys. Res. 87 (B11), 9329–9339. https://doi.org/10.1029/JB087iB11p09329.

Pruess, K., Narasimhan, T.N., 1985. A practical method for modeling fluid and heat flow in fractured porous media. SPE J. 25 (1), 14–26. https://doi.org/10.2118/10509-PA. SPE-10509-PA.

Ramirez, B., Kazemi, H., , Al-kobaisi Mohammed, Ozkan, E., Atan, S., 2009. A Critical Review for Proper Use of Water/Oil/Gas Transfer Functions in Dual-Porosity Naturally Fractured Reservoirs: Part I. SPE 109821-PA.

Ren, G., Jiang, J., Younis, R., 2017. Fully-Coupled XFEM-EDFM hybrid model for geomechanics and flow in fractured reservoirs. In: SPE 182726-MS.

Renard, P., de Marsily, G., 1997. Calculating equivalent permeability: a review. Adv. Water Resour. 20 (5—6), 253–278. https://doi.org/10.1016/S0309-1708(96)00050-4.

Sartori, A., 2018. Uncertainty Quantification Based on Hierarchical Representation of Fractured Reservoirs. MS Thesis. TU Delft, Delft, Netherlands. March 2018.

Sun, H., Yao, J., Gao, S., et al., 2013. Numerical study of CO2 enhanced natural gas recovery and sequestration in shale gas reservoirs. Int.x J. Greenhouse Gas Contr. 19, 406–419.

Tene, M., Bosma, S.B., Al Kobaisi, M.S., et al., 2017. Projection-based embedded discrete fracture model (pEDFM). Adv. Water Resour. 105, 205–216. https://doi.org/10.1016/j.advwatres.2017.05.009.

Voskov, D., 2012. An extended natural variable formulation for compositional simulation based on tie-line parameterization. Transport Porous Media 92 (3), 541–557. https://doi.org/10.1007/s11242-011-9919-2.

Wang, Y., Hajibeygi, H., Tchelepi, H., 2014. Algebraic multiscale solver for flow in heterogeneous porous media. J. Comput. Phys. 259, 284–303. https://doi.org/10.1016/j.jcp.2013.11.024.

Wang, K., Liu, H., Luo, J., Wu, K., Chen, Z., 2017. A comprehensive model coupling embedded discrete fractures, multiple interacting continua, and geomechanics in shale gas reservoirs with multiscale fractures. Energy Fuels 31 (8), 7758–7776, 2017.

Wang, C., Ran, Q., Wu, Y., 2019. Robust implementations of the 3D-EDFM algorithm for reservoir simulation with complicated hydraulic fractures. J. Petrol. Sci. Eng. 181, 106229.

Wang, C., Winterfeld, P., Johnston, B., Wu, Y., 2020. An embedded 3D fracture modeling approach for simulating fracture-dominated fluid flow and heat transfer in geothermal reservoirs. Geothermics 86, 101831.

Warren, J.E., Root, P.J., 1963. The behavior of naturally fractured reservoirs. SPE J. 3 (3), 245–255. SPE-426-PA.

Xu, J., Sun, B., Chen, B., 2019. A hybrid embedded discrete fracture model for simulating tight porous media with complex fracture systems. J. Petrol. Sci. Eng. 174, 131–143.

Yan, X., Huang, Z., Yao, J., et al., 2019. Numerical simulation of hydro-mechanical coupling in fractured vuggy porous media using the equivalent continuum model and embedded discrete fracture model. Adv. Water Resour. 126, 137–154.

Yao, J., Sun, H., Fan, D., et al., 2013. Numerical simulation of gas transport mechanisms in tight shale gas reservoirs. Petrol. Sci. 10 (4), 528–537.

Yu, X., Winterfeld, P., Wang, S., Wang, C., Wang, L., Wu, Y., 2019. A Geomechanics-Coupled Embedded Discrete Fracture Model and its Application in Geothermal Reservoir Simulation. SPE 193931-MS.

Zaydullin, R., Voskov, D.V., James, S.C., et al., 2014. Fully compositional and thermal reservoir simulation. Comput. Chem. Eng. 63, 51–65. https://doi.org/10.1016/j.compchemeng.2013.12.008.

Zeng, Q., Yao, J., Shao, J., 2018. Numerical study of hydraulic fracture propagation accounting for rock anisotropy. J. Petrol. Sci. Eng. 160, 422–432. https://doi.org/10.1016/j.petrol.2017.10.037.

Zhang, Y., Yu, W., Sepehrnoori, K., et al., 2017. A comprehensive numerical model for simulating fluid transport in nanopores. Sci. Rep. 7, 40507.

Zhu, G., Yao, J., Sun, H., et al., 2016. The numerical simulation of thermal recovery based on hydraulic fracture heating technology in shale gas reservoir. J. Nat. Gas Sci. Eng. 28, 305–316. https://doi.org/10.1016/j.jngse.2015.11.051.

Ţene, M., Wang, Y., Hajibeygi, H., 2015. Adaptive algebraic multiscale solver for compressible flow in heterogeneous porous media. J. Comput. Phys. 300, 679–694. https://doi.org/10.1016/j.jcp.2015.08.009.